

Exploiting nonlinear dynamics in a coupled-core fluxgate magnetometer

Adi R Bulsara¹, Visarath In¹, Andy Kho¹, Antonio Palacios²,
Patrick Longhini¹, Joe Neff¹, Gregory Anderson¹, Christopher Obra¹,
Salvatore Baglio³ and Bruno Ando³

¹ Space and Naval Warfare Systems Center San Diego, Code 2373, 53560 Hull Street, San Diego, CA 92152-5001, USA

² Nonlinear Dynamics Group, Department of Mathematics and Statistics, San Diego State University, San Diego, CA 92182, USA

³ Dipartimento di Ingegneria Elettrica Elettronica e dei Sistemi, Univ degli Studi di Catania, Viale A Doria 6, 95125 Catania, Italy

E-mail: bulsara@spawar.navy.mil, visarath@spawar.navy.mil, kho@spawar.navy.mil, palacios@euler.sdsu.edu, longhini@spawar.navy.mil, jneff@spawar.navy.mil, anderson@spawar.navy.mil, obra@spawar.navy.mil, salvatore.baglio@diees.unict.it and bando@diees.unict.it

Received 8 January 2008, in final form 22 April 2008

Published 12 June 2008

Online at stacks.iop.org/MST/19/075203

Abstract

Unforced bistable dynamical systems having dynamics of the general form $\tau_F \dot{x}(t) = -\nabla_x U(x)$ cannot oscillate (i.e. switch between their stable attractors). However, a number of such systems subject to carefully crafted coupling schemes have been shown to exhibit oscillatory behavior under carefully chosen operating conditions. This behavior, in turn, affords a new mechanism for the detection and quantification of target signals having magnitude far smaller than the energy barrier height in the potential energy function $U(x)$ for a single (uncoupled) element. The coupling-induced oscillations are a feature that appears to be universal in systems described by bi- or multi-stable potential energy functions $U(x)$, and are being exploited in a new class of dynamical sensors being developed by us. In this work we describe one of these devices, a coupled-core fluxgate magnetometer (CCFM), whose operation is underpinned by this dynamic behavior. We provide an overview of the underlying dynamics and, also, quantify the performance of our test device; in particular, we provide a quantitative performance comparison to a conventional (single-core) fluxgate magnetometer via a 'resolution' parameter that embodies the device sensitivity (the slope of its input–output transfer characteristic) as well as the noise floor.

Keywords: nonlinearity, coupling, magnetometer

(Some figures in this article are in colour only in the electronic version)

1. Introduction

A large class of dynamic sensors have nonlinear input–output characteristics, often corresponding to a bistable potential energy function that underpins the sensor dynamics. These sensors include magnetic field sensors, e.g. the simple (classical) fluxgate sensor [1–4] and the superconducting quantum interference device (SQUID) [5], ferroelectric sensors [6] and mechanical sensors [7], e.g. acoustic

transducers, made with piezoelectric materials. Fluxgate magnetometers, the focus of this work, have always been of interest to the technical and scientific communities as practical and convenient sensors for magnetic field measurements requiring a resolution around 1 μT at room temperature; they have found applicability [4, 8] in fields such as space and geophysical exploration and mapping, and non-destructive testing, as well as assorted military applications. Recently, the possibilities offered by new technologies and

materials in realizing miniaturized devices with improved performance have led to renewed interest in a new generation of cheap, compact and low-power fluxgate sensors. However, their miniaturization is complicated by the rapid increase of the magnetic noise with the reduction of the device dimensions, and general practical requirements for achieving high sensitivity (large number of windings, large cross-sectional sensor area and large driving current) which, however, are at odds with the desired characteristics (low cost, power and noise) of the miniaturized sensors. Nonetheless, despite the difficulties manifest in integrated devices with better performance, the literature does contain good examples of fluxgate sensors in PCB [9–11] and even CMOS [12, 13]. In particular, CMOS affords the possibility of realizing the sensing part (fluxgate) and the read-out circuit on the same chip, resulting in enhanced reliability, and lower costs in batch production. Today's highly specialized fluxgate devices boast laboratory noise floors as low as 10 pT/ Hz^{-1/2} [14], and are used in a variety of magnetic remote sensing applications [15].

The conventional (single-core) fluxgate magnetometer (SCFM) can be treated [17] as an overdamped nonlinear dynamic system by assuming the core as approximately single core-domain, and writing an equation for the evolution of the (suitably normalized) macroscopic magnetization parameter $x(t)$:

$$\begin{aligned} \tau_F \dot{x}(t) &= -\nabla_x U(x, t), \\ U(x, t) &= \frac{x^2(t)}{2} - \frac{1}{c} \ln \cosh c[x(t) + h(t)]. \end{aligned} \quad (1)$$

c is a nonlinearity parameter (proportional to the ratio T_c/T with T the temperature and T_c the Curie temperature) which controls the topology of the potential function $U(x, h(t) = 0)$: the system becomes monostable, or paramagnetic, for $c < 1$ corresponding to an increase in the core temperature past the Curie point, and remains ferromagnetic for $c > 1$. The overdot denotes the time derivative, and $h(t)$ is an external signal comprising a *known* time-periodic (sinusoidal or triangular) reference signal as well as the target signal ε (taken to be dc throughout this treatment). τ_F is the device time constant (inverse bandwidth); usually this time is very small, so that for most application scenarios, the device can be treated as a static nonlinearity. The known time-periodic signal switches the core magnetization between its stable steady states on a time scale given, roughly, by one-half the period of the signal. Then the target signal (which is, for the applications that concern us, too weak to overcome the energy barrier between the steady states) is quantified via its asymmetrizing effects on the system response. Good treatments of the conventional fluxgate magnetometer can be found in [1–4].

Usually, the amplitude of the bias signal is taken to be quite large, often far above the deterministic switching threshold which is itself dependent on the potential barrier height and the separation of the minima, in order to render the response largely independent of the noise. The frequency is also quite high (30–200 kHz in some commercial devices) in order to achieve good electromagnetic coupling among circuit elements, avoid the $1/f$ portion of the power spectral density (PSD) and ensure an adequate number of data points

for averaging purposes. Hence, the switching events are controlled by the bias signal. In the presence of background noise and absent the target signal, the PSD of the system response contains only odd harmonics of the (usually time-sinusoidal) bias signal. The effect of an additional target dc signal is, then, to skew the potential, resulting in the appearance of features at even harmonics of the bias frequency ω in the system response. Put succinctly, for an *a priori* symmetric potential function $U(x)$, the spectral amplitude at 2ω is zero unless the asymmetrizing dc signal is present, hence the appearance of power at 2ω and its subsequent analysis is used as a detection/quantification tool for the target signal.

An alternative to the power-spectral-based readout is a time-domain-based readout that relies on a compilation of the 'residence times' in the stable steady states; this procedure is the backbone of the readout scheme in our recently developed single-core fluxgate magnetometer (SCFM) [17, 19–21]. In the presence of a noise background, the crossing times have random components, and one must compute a noise-averaged residence time. The residence times readout has some advantages compared to the conventional (PSD based) readout scheme: it can be implemented experimentally without complicated feedback electronics, and works without the knowledge of the computationally demanding power spectral density of the system output (in most cases a simple averaging procedure on the system output works just fine) and, finally, it performs well in the presence of noise. The simplicity of the technique is underpinned by its *event-based* structure, akin to the occurrence of neural 'spikes' [16] with very little required knowledge of the system dynamics leading up to each spike; this is, truly, a discrete 2-state system replacement of the more complex potential-based dynamics so that relevant observable becomes the 'inter-spike interval', typically a random variable whose statistics impart all the relevant information about the stimulus and the system response to it. A variant of this readout was proposed for fluxgate sensors as early as 1961 [18].

One can show [19–21] (in contrast to the conventional readout scheme applied to the SCFM) that the sensitivity of the SCFM subject to the residence times readout is inversely proportional to the bias amplitude and frequency [20]. Hence, the (theoretical) conditions for increasing the sensitivity in the residence times readout correspond to those for decreasing the onboard power requirement. Of course, one cannot lower the bias amplitude and frequency too far; the frequency must remain high enough to ensure a good data sampling rate as well as strong electromagnetic coupling between the core and the readout circuit elements, while the amplitude must remain somewhat higher than the energy barrier height separating the steady states (i.e. the saturation states of the hysteresis loop) of the potential energy function, to ensure reliable switching in the absence of the target signal. Further, as the reference signal amplitude approaches the deterministic switching limit (the point at which the deterministic forcing alone is just sufficient to drive switching events) from above, the switching events become increasingly contaminated by the sensor noise floor, and a large number of crossing events must be gathered in order to obtain a reliable estimate for the difference in mean

residence times. Hence, in practical applications, the decrease in onboard power (with the concomitant decrease in the noise contribution from the bias signal generator) must be offset against an increase in the observation time, required to obtain reliable statistics [17].

Following the above preamble, this paper will focus on a novel class of magnetometers that use the (conventional) fluxgate element, i.e. the wound ferromagnetic core, as a component in a unidirectionally coupled nonlinear dynamic system. We organize this paper as follows: in the following section, we provide a brief theoretical overview of the coupled-core dynamics together with the emergent cooperative behavior that is exploited in the coupled-core system. Details of the calculations are not presented; they have already been published separately [22]. This is followed by the thrust of this paper: a description of the experimental setup and readout of the CCFM, and a compendium of results, aimed at demonstrating the validity of the theoretical model, and affording the possibility of detecting weak dc target fields, with significant performance enhancements over its SCFM counterpart. As part of our expose, we will introduce a performance measure that embodies the (appropriately defined) sensitivity of the device as well as the effect of system fluctuations on the response.

2. Coupled-core fluxgate magnetometer (CCFM)

We start with an overview of the coupling scheme including a new twist which we have, recently, implemented in our laboratory CCFM. We give theoretical expressions for the threshold for the onset of coupling-induced cooperative behavior characterized by oscillations, as well as their frequency without, however, giving many details of the derivation, since this has already been done in prior work. We then describe the implementation of the coupled-core sensor, and show that the experimental setup does, in fact, yield the correct physical results predicted by the theory. Finally, we quantify the sensor performance within the reference frame of the SCFM (we provide the main figures of merit of our SCFM for reference), and buttress our preference for this sensor (over the SCFM) despite somewhat greater engineering complexity.

2.1. Background: coupling scheme and dynamics

The CCFM is constructed by *unidirectionally* coupling $N (> 2)$ wound ferromagnetic cores with cyclic boundary condition, thereby leading to the dynamics,

$$\dot{x}_i = -x_i + \tanh(c(x_i + \lambda x_{i+1 \bmod N} + \varepsilon)), \quad i = 1, \dots, N \quad (2)$$

where $x_i(t)$ represents the (suitably normalized) magnetic flux at the output (i.e. in the secondary coil) of unit i , and $\varepsilon \ll U_0$ is an external dc ‘target’ magnetic flux, U_0 being the energy barrier height (absent the coupling) for each of the elements (assumed identical for theoretical purposes). Note that the (*unidirectional*) coupling term, having strength λ , which is assumed to be equal for all three elements, is *inside* the nonlinearity, a direct result of the mean-field nature of

the description (the coupling is through the induction in the primary or ‘excitation’ coil). The dynamics of this coupled system have been detailed in [22] where it is shown that the oscillatory behavior occurs even for $\varepsilon = 0$, however when $\varepsilon \neq 0$, the oscillation characteristics change; these changes can be exploited for signal quantification purposes, the underpinnings of the CCFM. Note the absence of the bias signal (that is endemic to the SCFM) in the dynamics (2); in the coupled-core system, the oscillations (corresponding to switching events in each core between the allowed stable states) are generated by the coupling and the cyclic boundary condition. We also observe that the particle-in-potential paradigm is no longer applicable to the coupled system (2) due to the unidirectional coupling. Finally, we note that the oscillations occur for any $N \geq 3$, however we concentrate on the $N = 3$ case for convenience (the results for a general odd N can be readily written down by inspection [22]). Also, N can be even, however in this case one must have a large number of coupled elements [23]. The above system (with $N = 3$) has been realized in the laboratory [22] and is, currently being implemented in a cheap, lightweight, room temperature magnetic sensor, the CCFM.

A theoretical analysis [22] shows that the system (2) exhibits coupling-induced oscillatory behavior with the following features:

- (1) The oscillations commence when the coupling coefficient exceeds a threshold value

$$\lambda_c = -\varepsilon - x_{\text{inf}} + c^{-1} \tanh^{-1} x_{\text{inf}}, \quad (3)$$

with $x_{\text{inf}} = \sqrt{(c-1)/c}$; note that in our convention, $\lambda < 0$ so that oscillations occur for $|\lambda| > |\lambda_c|$.

- (2) The individual oscillations (in each elemental response) are separated in phase by $2\pi/N$, and have period

$$T_i = \frac{N\pi}{\sqrt{c}x_{\text{inf}}} \left(\frac{1}{\sqrt{\lambda_c - \lambda}} + \frac{1}{\sqrt{\lambda_c - \lambda + 2\varepsilon}} \right) \quad (4)$$

which shows a characteristic dependence on the inverse square root of the bifurcation ‘distance’ $\lambda_c - \lambda$, as well as the target signal ε ; these oscillations have been experimentally produced at frequencies ranging from a few Hz to high kHz.

- (3) The *summed* output oscillates at period $T_+ = T_i/N$ and its amplitude (as well as that of each elemental oscillation) is *always suprathreshold*. This latter consideration implies that the external bias signal used in the single core fluxgate [19] is no longer needed to drive the magnetization between its saturation states. Increasing N changes the frequency of the individual elemental oscillations, but the frequency of the summed response is seen to be *independent* of N . Numerical simulations of the system (2) have verified the characteristic scaling of the period with the square root of the ‘bifurcation distance’ $\lambda_c - \lambda$. As expected, decreasing the coupling strength increases the oscillation period.
- (4) Changing the target field strength also changes the period, via its influence on the threshold λ_c ; in addition, we immediately observe that increasing ε leads to λ_c going to larger (and negative) values i.e. a larger $|\lambda|$ is required

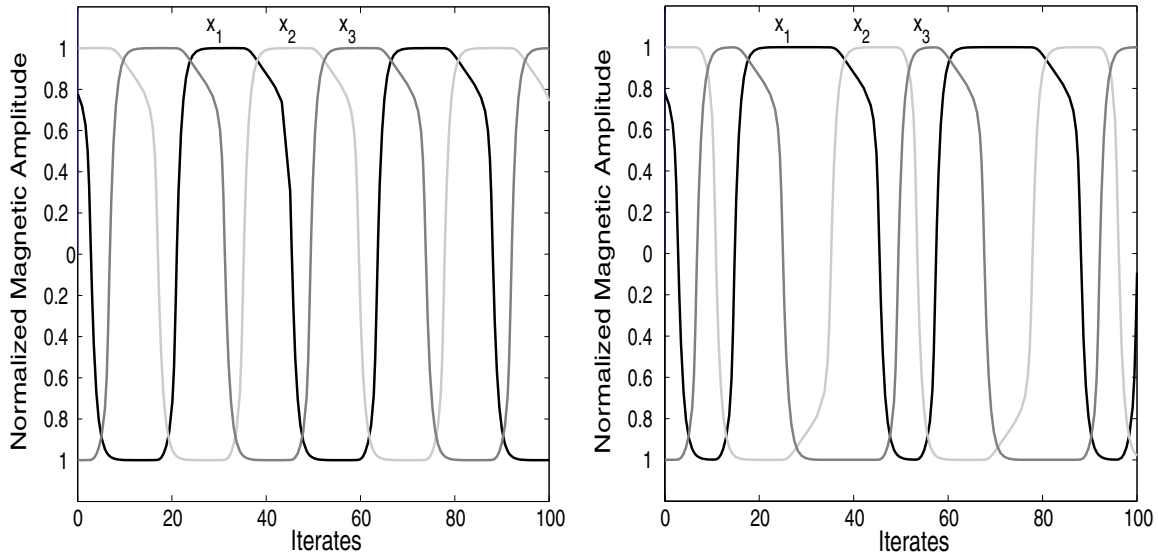


Figure 1. Time series from simulations on a standard CCFM arrangement (left) and AO arrangement (right). The RTD $\Delta_1(t)$ (see text) of the element x_1 in the AO arrangement, is seen to be N times the corresponding quantity in the standard arrangement. $N = 3$, $c = 3$, $\lambda = -0.54$, $\varepsilon = 0.07$.

to drive the system past its critical point. A glance at Ref period quickly confirms that for a fixed coupling strength, a critical value $\varepsilon_c = |\lambda_{c0} - \lambda|$ will render the period imaginary; effectively, the oscillations are suppressed at this value of the applied signal. Here, we have defined $\lambda_{c0} = -x_{\text{inf}} + c^{-1} \tanh^{-1} x_{\text{inf}}$ as the critical coupling value, absent a target signal.

- (5) Finally, it is important to observe that the elements in the ring switch *sequentially* between their stable steady states. This is apparent in figure 1 (left panel) which shows that during the switching interval for any of the elements, the other two elements remain in their (opposite) steady states, this gives the emergent oscillations the appearance of a ‘ripple’ (visually, reminiscent of a soliton) that propagates around the ring.

In practice, it is usually more convenient to use the *residence times difference* (RTD) Δt as a quantifier of the target signal. In the hypothesis made here of static hysteretic nonlinearity, the RTD quantifies the difference between the times spent by the magnetization state variable in each stable state. The RTD can be computed [22], from the i th core element output signal, as

$$\Delta t = \frac{\pi}{\sqrt{cx_{\text{inf}}}} \left(\frac{1}{\sqrt{\lambda_c - \lambda}} - \frac{1}{\sqrt{\lambda_c - \lambda + 2\varepsilon}} \right), \quad (5)$$

which vanishes (as expected) for $\varepsilon = 0$. The system responsivity, defined via the derivative $\partial \Delta t / \partial \varepsilon$, is found to increase dramatically as one approaches the critical point in the oscillatory regime; this suggests that careful tuning of the coupling parameter so that the oscillations have very low frequency, could offer significant benefits for the detection of very small target signals. In this regime, one may do a small- ε expansion to yield $\Delta t \approx \pi \varepsilon (cx_{\text{inf}})^{-1/2} (\lambda_{c0} - \lambda)^{-3/2}$, where λ_{c0} now represents the critical coupling, absent the target signal. The responsivity, defined via the RTD Δt , is seen to be (for small ε) *independent* of ε , a considerable

advantage when trying to optimize the device for maximal responsivity; by contrast, if one computes the responsivity via the change in oscillation period with ε , it becomes apparent that the responsivity depends on ε . For a fixed ε one observes, immediately, that the responsivity $\partial \Delta t / \partial \varepsilon$ increases as one approaches the critical point (through adjusting the coupling parameter λ), i.e. the instrument yields its optimal performance in the very low-frequency regime, close to the oscillation threshold. In this context, it is worth noting that the experimental system can be made to oscillate at very low frequencies, far lower than the bias frequency that is necessary for the readout of conventionally operated (single core) fluxgates. This ‘tunability’ of the optimal operating regime, if done carefully with consideration of the magnitude of target signals expected in a given application, is a big advantage of the coupled system over its single element counterpart. It immediately removes the onboard power requirement for the bias signal generator that is integral to the SCFM, although this power savings is offset, somewhat, by the power that must be supplied to the coupling circuit elements. In addition, a significant source of noise (the bias signal generator) is eliminated. It is always important to realize that, in the coupled system, the assorted circuit components (in particular those that realize the coupling circuit) do require an onboard power source; hence the emergence (and sustenance) of the oscillations does not violate any fundamental laws. With the cyclic boundary condition and the appropriate choice of coupling strength, the only remaining condition for the oscillatory behavior is that at least one element should have an initial state that is different from the others; this is quite easy to achieve in practice, since the initial conditions are random in any reasonable device. On connection, the onset of oscillations is quite rapid; once a given elemental state variable x_i has made a single interval switch, it continues to oscillate.

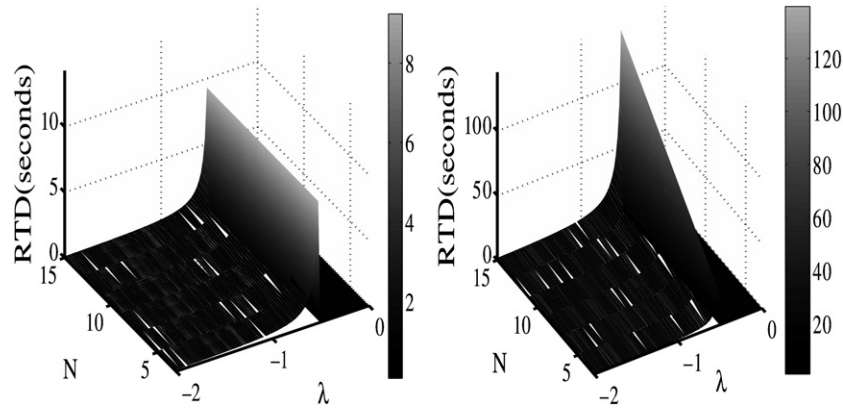


Figure 2. RTD response (Δt) of the x_1 element in a CCFM as a function of ring size N , and coupling strength λ . (Left) standard configuration (SO) and (right) alternating configuration (AO). Near the onset of coupled-induced oscillations, in particular, the RTD response of the standard configuration remains constant (as expected) while that of the AO configuration increases linearly as a function of N . $c = 3$, $\varepsilon = 0.07$. In each case, the maximum RTD is realized infinitesimally past the critical coupling λ_c . The response has been computed, in both figures, via a numerical integration of the full system dynamics (2) and (6). Note the (substantial) difference in the vertical scales.

A recent twist to the above coupling scheme has led to a substantial improvement in the performance of the CCFM. The idea is to reverse the orientation of successive cores so that the sign of the ε term in (2) alternates; for N odd, this guarantees that there will be two adjacent elements with the same sign of ε . This alternating orientation (AO) arrangement is described by:

$$\dot{x}_i = -x_i + \tanh(c(x_i + \lambda x_{i+1 \bmod N} + (-1)^{i+1} \varepsilon)), \quad i = 1, \dots, N. \quad (6)$$

One can readily calculate [24] the oscillation period T_i of an individual element as well as the threshold value λ_c^{AO} for the onset of oscillations; these quantities are identical to those given above for the conventional arrangement. However, this does not apply to the residence times difference. We find that this quantity changes, depending on the particular element under consideration. Focusing on the element $i = 1$ which has the same sign of ε as the element that it is back-coupled to (namely the $i = 3$ element), we find [24]:

$$\Delta_1 t = N \Delta t \quad (7)$$

with the result generalized to the arbitrary N (odd) case. This departure from the standard behavior in the arrangement (2) is evident in figure 1. In fact, recalling that $\partial \Delta t / \partial \varepsilon$ measures the responsivity (often called the sensitivity) of a CCFM, it follows that the sensitivity of the AO configuration, using $x_1(t)$ as the measurement element, improves, linearly, by a factor of N when compared to the best sensitivity that can be achieved by the standard CCFM configuration, given the same external signal and core parameters. The dependence of the RTD and, consequently of the sensitivity, on the size (i.e. number of coupled dynamic elements) of the ring in the AO configuration is in direct contrast to the sensitivity response of the standard configuration, in which increasing N beyond $N = 3$ does not lead to additional benefits. The above observations are confirmed in figure 2, in which we calculate, numerically, the RTD $\Delta_1 t$ for a CCFM system with standard as well as with AO configuration. As expected, near the onset of coupling-induced oscillations, the RTD response of the $i = 1$ element

in a standard CCFM configuration remains constant while that of the AO configuration increases, linearly, with N .

It is clear that, for rings of arbitrary N (odd) elements, one always has a situation wherein two adjacent elements have the same orientation (i.e. the sign of the dc term in the dynamics (6) is the same for these two elements). In this case, the most sensitive (i.e. yielding the largest RTD) element is always the one (out of these two elements) which receives input from an element with the opposite orientation. For example, in the system at hand, x_3 and x_1 have the same orientation, with x_3 receiving input from x_1 (same orientation) but x_1 receiving input from x_2 (opposite orientation); hence, for the $N = 3$ configuration being considered here, x_1 is the most sensitive for detecting the target dc signal via the RTD.

2.2. Laboratory implementation of the CCFM

The experimental coupled core device involves three ferromagnetic cores together with the coupling circuit; the setup conforms to the model equations (2); in recent experiments we have also implemented the AO arrangement (6) which affords the prospect of enhanced sensitivity. Figure 3 shows the block diagram, as an overview, of the setup. We now provide some details of the construction of the sensor and the coupling circuit. The microwire-fluxgate magnetometer is based on 100 μm FeSiB amorphous ferromagnetic core material. The ferromagnetic cores are produced by rapidly cooling alloys comprised of 80% Fe, Ni or Co, and 20% P, Si, Al, C, B to obtain the desired magnetic properties [25]. In particular, the FeSiB microwire is obtained using the in-water quenching technique with a typical diameter range of 80–160 μm and cylindrical structure. Typically, the solidification process induces two magnetic domain regions: (1) an inner core, easy axis parallel to the wire axis and (2) an outer shell with radial easy axis. The internal stress induced by the solidification process can be reduced through an annealing process at 350–400 $^\circ\text{C}$. The (wound) core implementation can, then, be summarized as follows: (1) 100 μm diameter wire-coils (primary and secondary coils) are wound around a plastic

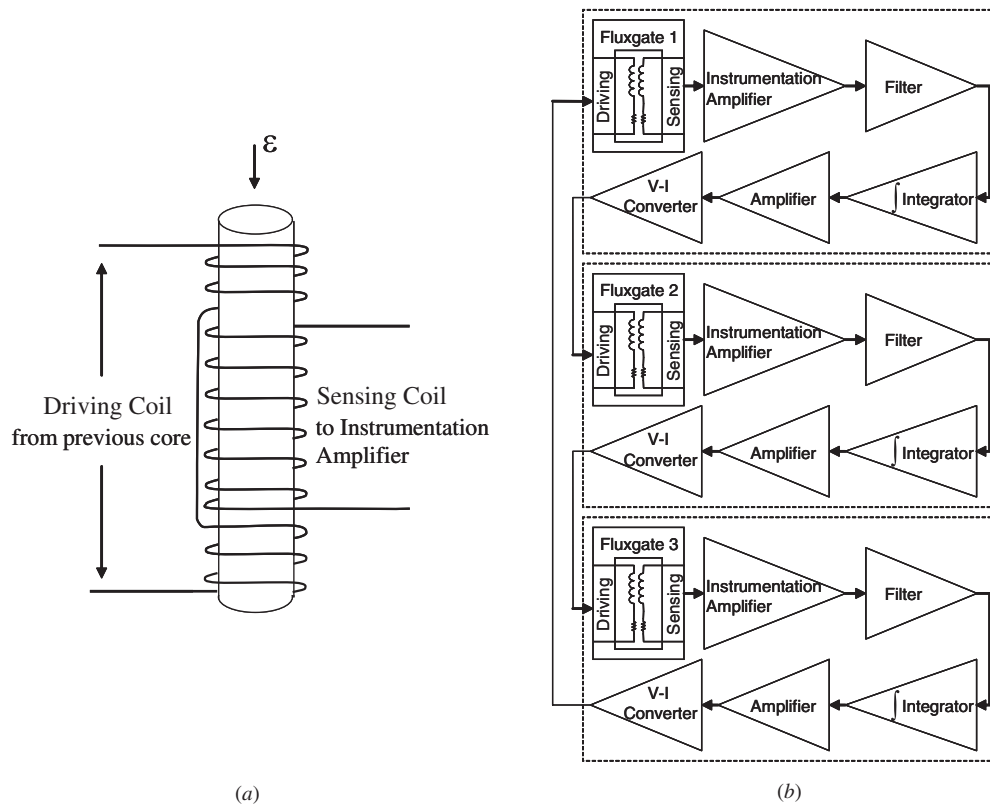


Figure 3. (a) Schematic representation of a single ferromagnetic core. (b) Flow diagram of the $N = 3$ coupled-core system as an overview for the device realization. The AO configuration is achieved by crossing wires at the connector between the x_2 output and the coupling circuit.

structure (of diameter 1.2 mm) and (2) a cylindrical glass-support (1 mm external radius and $100 \mu\text{m}$ internal radius) is used to contain the $100 \mu\text{m}$ FeSiB fluxgate core.

The cylindrical glass-support is fixed to the center of the solenoid and the magnetic core is centered with respect to the cylindrical plastic support. The cores are mounted on the faces of a structure with a triangular section for orienting all of them in the same direction (the device is, effectively, a single-axis sensor with the target field measured along each core axis) and then coupled through electronic circuits wherein the voltage readout (i.e., the time derivative signal of the flux detected by one of the sensing coils) is amplified by a voltage amplifier (see figure 3). Next, the signal is passed through an integrator to convert the derivative signal seen by the sensing coil back to the 'flux' form so that the experimental system closely conforms to the model. The signal then passes through an amplifier to achieve adequate gain to drive the adjacent fluxgate. Following this, the signal passes through a voltage-to-current converter ($V - I$ converter) in its final step to drive the primary coil of the adjacent fluxgate. The setup is repeated for the other two coupling connections for the remaining cores and all values of the coupling circuit parameters are closely matched from one set to the other. Each stage of the coupling circuit also employs low noise, high speed and high precision operational amplifiers (op-amps) to minimize the time delay in order to conform closely to the model since a knowledge of the state variable x_i is available instantly in the model. Note that, starting from the standard configuration, the AO configuration

is achieved by reversing the polarities of the excitation coils for the x_3 coil; this can be, simply, achieved by crossing wires at the connector between the x_2 output and the coupling circuit.

A stability analysis of the model equations with respect to a delay in the signal shows no significant divergence in the behavior, if the delay time is limited to 10% of the oscillation period. This point is very significant in the implementation of the actual device because there will always be delays in the electronic circuits due to the component response times, and the coupling circuit board presented here has about 2–4% of the period in delay time (depending on the choice of op-amps, resistors and capacitors used) when operating at a relatively high frequency (around 150 Hz). Most of the time, the laboratory device has been operated in the 37–100 Hz regime, so that the delay is even smaller.

Once the magnetometer is configured, as described above, the outputs of the coupled cores are sent for processing to extract the information about the target field being detected. The signal from the inverted core element is passed through a Schmitt trigger which converts the output into a clean dichotomous signal, retaining only the all-important information about the locations (along the time axis) of the switching events. The output from the Schmitt trigger is passed through a voltage divider and diode to convert the signal to TTL in which +5 V corresponds to a HIGH and 0 V corresponds to a LOW. This HIGH and LOW state is then passed to a programmable integrated circuit (PIC) microcontroller for further processing; this, eventually, leads to compilation of the residence times T_{\pm} in the upper and lower states.

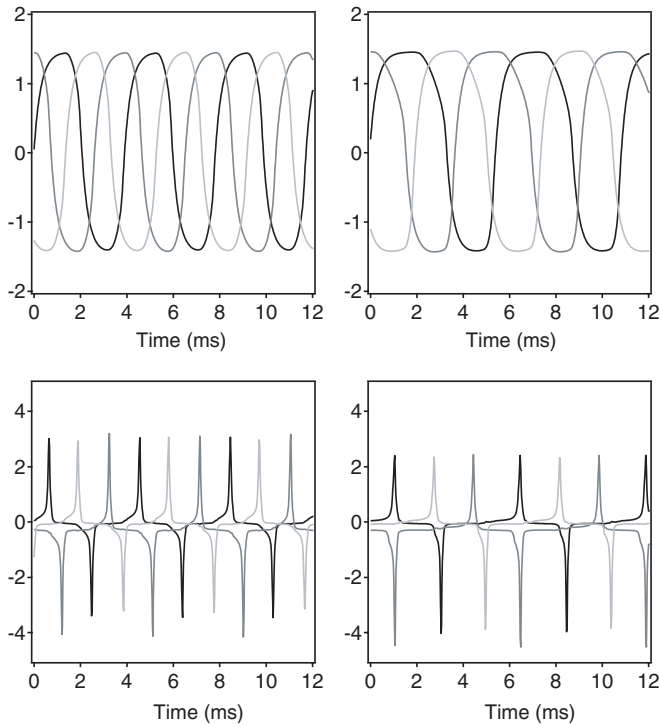


Figure 4. Time series from the experimental system (standard configuration) for $\varepsilon = 0$ (left column) and $\varepsilon = 8.0 \mu\text{T}$ (right column). The top figures show the input (i.e. response) signal fed to each core. It can be observed as the (oscillatory) traveling wave pattern discussed in the text. Each one has the same amplitude and frequency but each is phase shifted by 120° as observed in the numerical model. The bottom figure shows the outputs (transduced into voltages) of the sensing coils of each core; the signals are recorded after the instrumentation amplifier stages. The response matches, qualitatively, the theoretical results derived earlier [22]. $G = -0.8$ in both cases.

In practice, both the upper and lower residence times are accumulated for an appropriate number (10–15 in our laboratory setup, but adjustable, depending on the circumstances of the application) of oscillation cycles. A mean and a standard deviation are then computed for both. The difference $T_+ - T_-$ of the two mean values is proportional to the external field in the small- ε limit, as already noted in section 1. Since there is inherent noise within the system, the standard deviation is always nonzero for both residence times.

2.3. Experimental results

The oscillations observed from our coupled setup are quite striking (figure 4). The system readily oscillates in a traveling wave pattern and, like the model, it favors this pattern no matter how many times it is restarted. The oscillation frequency, for the system parameter values considered in this case is about 260 Hz. Each wave is phase shifted by exactly $\frac{2\pi}{3}$ as predicted by the model. Comparison of the experimentally obtained oscillations to the numerical results (as shown in figure 1) shows good agreement with the caveat that, since the values of c and the time constant τ_F in the actual device (we set $\tau_F = 1$ [s] in the model) are not known, we cannot correctly compare

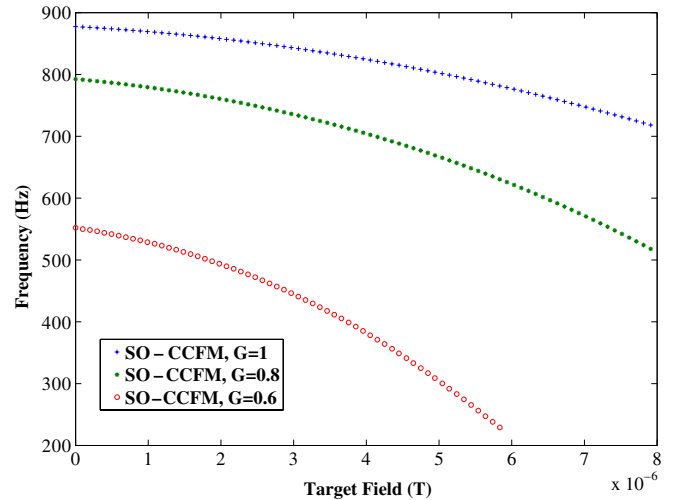


Figure 5. Experimentally obtained frequency scaling with respect to the coupling strength, expressed as a gain and the applied dc target magnetic field (horizontal axis). The curves scale as $\sqrt{\lambda_c - \lambda}$ in accordance with the theory.

the time scales in the model and the experimental observations. The amplitudes of the oscillations in the experiment are also arbitrary in comparison to the model because the recorded voltages depend on the gains set in the coupling circuit. The magnetic flux in the model saturates between ± 1 , but in the devices this quantity cannot be measured directly. We note that, despite the above issues, the qualitative agreement between theory and experiment is very good; in fact, all the mathematical relations listed in section 2 are well satisfied by the experimental data.

Further illustration of good qualitative agreement between the numerical system and the prototype system is the frequency scaling (figure 5), as a function of the coupling strength and also as a function of the applied (dc) field. As expected, the frequency of the coupled system should rise as the square root of the coupling strength; further, as the applied field magnitude increases, the frequency decreases until the coupling strength is at the critical value where the oscillations cease to exist. Increasing the coupling values beyond this point will not produce any oscillation. We recall that, in the convention adopted in our theoretical description, the coupling is *negative*, so that an ‘increase’ of coupling implies that the coupling coefficient λ approaches zero. Similarly, increasing the applied field in either direction away from zero will reduce the frequency of the oscillations as predicted by the model; this can also be observed in the experimental results shown in figure 5. The oscillations cease to exist when the applied field is too large because the field moves the system past the critical point into the non-oscillating regime; this behavior has already been outlined in the preceding section. In what follows, to facilitate the correspondence between theory and experiment, we adopt a notation wherein the coupling strength λ is expressed as $\lambda = \lambda^* G$ where λ^* is a constant parameter and G is the (dimensionless) gain of the amplifier (see figure 3) that can be tuned via the ratio of two resistors. Figure 6 (left) shows a family of responsivity curves as a function of the applied field for different coupling strengths; the figure agrees

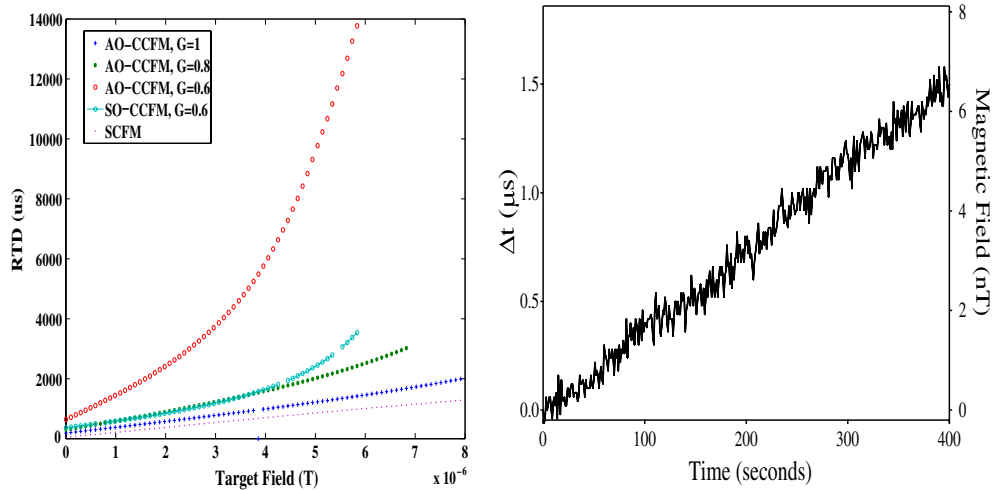


Figure 6. (Left panel) responsivity curves, of the residence time difference (RTD) versus the applied target magnetic field ε for different coupling strengths. As expected, the coupled-core system is less responsive as the dimensionless coupling parameter G is increased. In particular, note the large difference in responsivity (for the same $G = 0.6$) between the AO (top curve) and SO (second curve from top) configurations. The bottom curve is the responsivity of an ‘equivalent’ single core fluxgate magnetometer with bias signal amplitude selected to be slightly suprathreshold, thereby yielding the maximal sensitivity. (Right panel) temporal variation of the RTD response of the ‘preferred’ element (x_1 in figure 1(right)) as the target signal is swept (in 100 pT steps) through a range of values. $G = 0.8$.

well with theoretical results (not shown). As the coupling strength is increased toward the critical value, the responsivity curve becomes steeper. The greatest sensitivity is realized when the coupling strength is set closest to the critical value, but in this regime it can only detect a very small target field amplitude. Hence, the ability to tune the coupling to detect a range of target field strengths, must be a central feature of this mode of operation; when implemented, it presents a capability where one may tune the coupling to reduce the sensitivity and increase the operating range, or vice versa. The RTD response (of a single element in the AO configuration) as a function of the target signal for a particular value of the coupling strength is shown in figure 6 (right). In the context of this figure it must, of course, be remembered that the RTD vanishes in the absence of the external signal.

3. Quantifying the sensor performance

It is appropriate to discuss the effect of the sensor noise floor on the response; in a real application, this noise can arise from internal (materials, electronics, etc) sources, as well as contamination of the target signal. The voltage output signal from a single core fluxgate (operated via the residence times readout) has been shown [19, 20] to have a noise component that can be well approximated by a Gaussian distribution. However, the individual residence times have noise components which are, in general, non-Gaussian; they have noise-dependent tails and, with increasing noise intensity the tails get longer, a feature that is quite common to two-state devices. Our earlier theoretical [17] and experimental [26] work on the SCFM showed these features, and also showed that decreasing the noise intensity (alternatively, increasing the bias amplitude A) reduced the tail and made the distributions more Gaussian-like; in the small σ^2/A limit (where σ^2 is a theoretical noise variance) the residence times distributions

are Gaussian [17], as also observed in the experiments. Of course, this comes at the price of reduced sensitivity (since the sensitivity, for the residence times readout, is inversely proportional to the bias amplitude). The above ratio can be reduced (for a given noise floor) by increasing the bias amplitude A , but this increases the onboard power as well as the contribution to the noise floor arising from the reference signal generator. A careful optimization of geometrical and other core parameters is also known to lower the noise in the voltage signal (see, e.g., [27]).

To better understand the ramifications of background noise, we have introduced [17] the (critical to a practical system) observation time T_{ob} , and defined a response signal-to-noise ratio (SNR) which is directly proportional to $\sqrt{T_{\text{ob}}}$. A longer observation time leads to an enhanced response (to very weak target signals), however, practical constraints may limit T_{ob} . One can increase the bias frequency ω , thereby increasing the number of crossing events and improving the statistics of the measurement process, however this implies a larger power requirement. Hence, in a practical application, one must strike a balance between the physical constraints (e.g. onboard power, noise from the bias signal generator) and the need to carry out a reliable measurement of the mean RTD . The practical configuration is also, of course, heavily dependent on the amplitude (relative to the energy barrier height) of the target signal ε to be quantified; it helps to have an *a priori* idea of the range of target signals under consideration for a given application. However, if the target signal is larger than the energy barrier height (or, roughly, the coercive field) it is, usually, easier to detect it by standard techniques that do not require a sophisticated sensor such as the one described in this work.

In the RTD readout the effects of noise are, usually, manifest in uncertainties in the crossing times at the lower and upper thresholds. The ensuing uncertainty (in the time-domain) has been, formally, connected [20] to an uncertainty

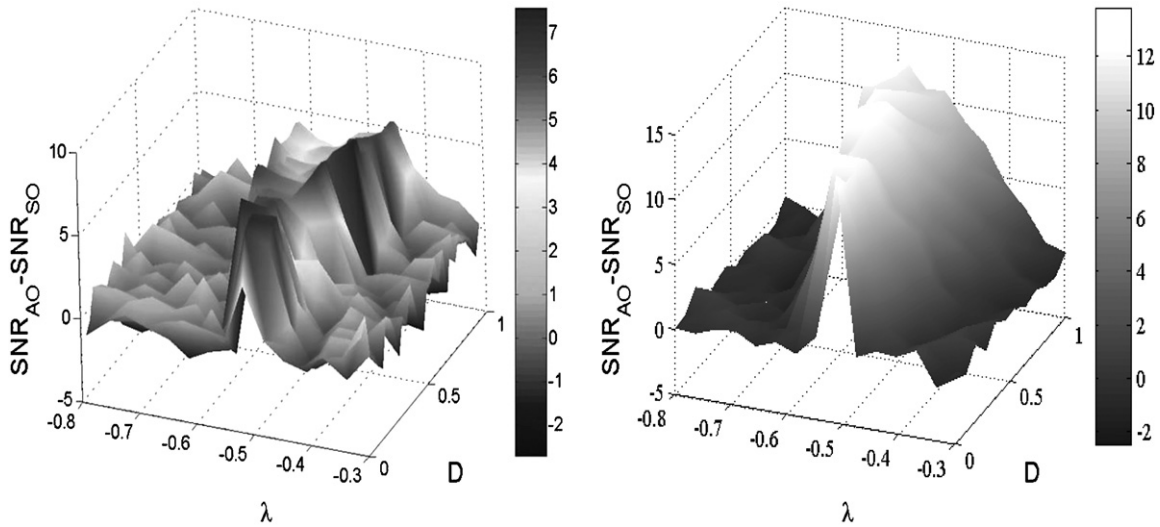


Figure 7. Difference in SNR response between alternating (AO) and standard (SO) core configurations as discussed in section 2 and figure 1. Observe that near the onset of coupling-induced oscillations the SNR response of the AO configuration is significantly better. The maximum SNR in each case is obtained just barely past the critical point (defined by λ_c). Parameters are: $N = 3$ cores (left panel) and $N = 7$ cores (right panel), $c = 3$, $\tau_c = 150.0$ and $\epsilon = 0.07$. In each case, the SNR has been measured for the element with the maximal response (see the text), at the feature corresponding to the oscillation frequency in the output power spectral density. Here, $D \equiv \sigma^2 \tau_c$ is the noise intensity parameter (see the text).

in the amplitude domain i.e., to an equivalent noise-floor [4] that one would obtain via an output power spectral density.

3.1. The effects of noise in the CCFM: an overview of recent results

Before introducing a performance-quantification measure specific to our time-domain readouts, we give a rapid overview of existing results on the effects of noise in the coupled-core device. This noise can arise from a contamination of the external target signal, as well as from the readout electronics, magnetic core, etc. Regardless of the source of the noise, we have treated it as being Gaussian band-limited noise having zero mean, variance σ^2 and correlation time (inverse bandwidth) τ_c , i.e. $\langle N(t) \rangle = 0$, $\langle N(t)N(t') \rangle = \langle N^2(0) \rangle \exp[-|t-t'|/\tau_c]$, with $\langle N^2(0) \rangle = \sigma^2 \tau_c / 2$; the ‘white’ limit of delta-correlated noise is realized for $\tau_c \rightarrow 0$.

A small *additive* noise floor (arising from internal sources) manifests itself in fluctuations of the ‘rest’ states of each core, about the deterministic mean values $\pm b$ (the minima of each core potential energy function, in the absence of coupling). Numerical simulations [28] of the coupled system, for this case, show that the threshold crossings are quite sharp and unambiguous in the presence of this noise term, as long as the noise is not too strong; this is a direct consequence of the very low time constant τ_F (usually $\ll \tau_c$) of each core; to all intents and purposes, each element behaves like a static nonlinearity, with near-instantaneous switching events.

We now consider the situation wherein the target dc signal is noise-contaminated. In this case, one inserts a correlated noise term $N(t)$ (specified as described above) additively into the argument of the nonlinearity in each of the equations (2) and (6). Our simulations in this case [24] have focused on a comparison of the spectral response (quantified by a SNR

obtained at the spectral feature at the switching frequency in the oscillatory regime), the intention being to compare the response of the two coupling configurations (2) and (6). These comparisons are well summarized in figure 7 wherein we plot the SNR difference (at the oscillation frequency) between the SO and AO configurations (given by (2) and (6), respectively). One readily finds that the AO configuration provides far better SNR performance when operated close to the onset of switching, i.e. in the low-frequency oscillation regime just past the critical point. The improvement is enhanced for increasing N . The AO configuration, therefore, offers a tangible way of improving the sensor responsivity (or resolution) by exploiting large- N effects, although any potential improvement must be balanced against the engineering complexity involved in producing a larger (than $N = 3$) device.

3.2. A performance measure: the resolution

The RTD readout that we use in our devices is very simple to implement; one requires a clock and a counting circuit to keep track of the crossing events of the upper and lower thresholds, and a running arithmetic mean of the residence times in the up and down states. The (measured) quantity of interest is, then, the mean RTD, denoted by \overline{RTD} .

We now introduce the ‘Resolution’; it is the minimum magnetic field that can be discriminated by the sensor against the background, after ambient static (homogenous) magnetic fields have been nulled out, as described earlier. The resolution is defined as

$$R = STD(\Delta_1 t) / [\partial \overline{\Delta_1 t} / \partial \epsilon] \quad (8)$$

where $\overline{\Delta_1 t}$ represents the averaged RTD measured (in this case) at the x_1 element and the denominator is simply the slope of the output–input transfer characteristic (the plot of $\overline{\Delta_1 t}$ versus

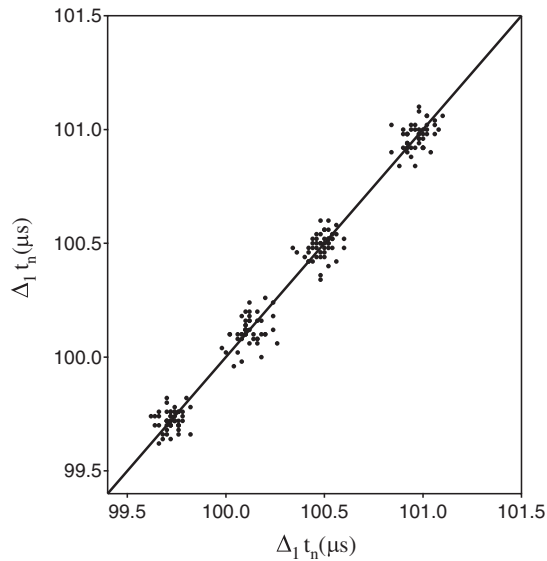


Figure 8. Return map of the (experimentally obtained) RTDs; each cluster corresponds to a different ε and the straight line is the locus of the means. Each individual point in a cluster corresponds to an average of 15–20 values of the RTD taken in an observation time window (0.1 s in this case). Standard deviation of each cluster is a function of ε (see the text), while mean value is proportional to ε so that the responsivity (denominator of (8)) is an ε -independent number (see the text). At low signal values, the resolution is, approximately, constant (see the text). Parameters are: $N = 3$ cores and $G = -0.8$.

the target signal ε), and represents the device responsivity. For small target signals, we expect this slope to be independent of ε (i.e. $\Delta_1 t \propto \varepsilon$); this is, of course, convenient for practical applications. The numerator in (8) is the standard deviation of the RTD, i.e., $STD(\Delta_1 t)$.

We now describe how this quantity is measured, experimentally, in a CCFM consisting of $N = 3$ cores following the AO dynamics (6), i.e., the ‘favored’ element for measuring the RTD is $x_1(t)$. We use an observation time (once the ambient static magnetic field nulling has been achieved) of 0.1 s and an oscillation frequency that is adjusted (via the coupling λ) to yield 15–20 cycles of the response during this observation window. Of course, the observation time can be increased, but this would depend on the circumstances of the particular application and, more importantly, on the statistics and stationarity (or lack thereof) of the ambient noise. Keeping ε fixed, we compute the time-averaged RTD $\Delta_1 t$ by averaging the RTDs obtained in the observation window. The experiment is then repeated several times for the same ε ; each repetition yields a time-averaged (over the observation window) RTD which is not necessarily the same as the others, due to fluctuations. In this way, one obtains a large number of time-averaged RTDs corresponding to the fixed value of ε . The quantity $\overline{\Delta_1 t}$ is, then, the statistical average of these points (for the same value of ε). The process is repeated for different values of ε . A plot of $\Delta_1 t$ versus ε shows clusters of discrete points (each point corresponding to an average over the observation window) for each value of ε . The locus of the statistical means of each cluster of points then yields a straight line for small ε . In figure 8, we have plotted the ‘return

map’ of the (experimentally obtained) RTDs. For a given ε , each data point in a cluster represents the (window-averaged) RTD at two successive observation intervals each 0.1 s long; thus, we generate a cluster of points corresponding to a plot (actually a residence times return map) of $\Delta_1 t_{n+1}$ versus $\Delta_1 t_n$. Each cluster of points corresponds to one value of the target field ε (in the absence of background noise, each cluster would collapse into a single point for that particular value of ε); in this experimental sequence (figure 8), the point clusters correspond to values of ε that are approximately 2.0 nT apart; one can use a smaller separation of ε values, however this separation has been chosen for purposes of elucidation (with smaller separation the clusters tend to merge into one another). The density function of each cluster is near-Gaussian, with a mean value corresponding to the averaged RTD over all the discrete points, and a standard deviation that can be computed from the observations. The locus of the mean values is the straight line. When one plots these mean RTD values as a function of ε (not shown), the slope of this line (the responsivity, i.e. the denominator of (8)) is 229.83 s T^{-1} . In the figure, the standard deviations of the point clusters are (from left to right) 0.057 315, 0.054 994, 0.065 573, 0.044 63 μs , resulting in resolutions (calculated from (8)) of 250, 240, 286, 195 pT respectively, resulting in a mean resolution of 242 pT for this particular realization of the sensor. The resolution is approximately constant (the deviations arise from experimental uncertainties and fluctuations) in this regime of low target signal. It is important to realize that, as ε increases, the target signal becomes more easily ‘resolved’. However, the analytic description of the response breaks down when ε becomes comparable to (or exceeds) the energy barrier height of a single element (isolated) potential function; in this regime, the resolution becomes ε -dependent.

One expects, at least in the linear regime ($\varepsilon \ll \Delta U$, the energy barrier height of a single isolated element), that the distribution of the discrete points corresponding to a given ε will be near-Gaussian; this is, in fact, observed in our experiments. The numerator in (8) is also computed, directly from the data, for each value of ε . The definition (8) should be compared with our heuristic definition of a response SNR [17]; we find, in fact, that the resolution is proportional to the inverse of the SNR. This is reasonable because a lower value of the resolution implies better performance, as does a higher value of the SNR. What is important to note is that the quantity in (8) incorporates the effects of the noise on the sensor performance in a simple manner that can be easily implemented in practice; we can, in fact, use this quantity to make comparisons between different sensor versions.

In an experiment, however, one cannot pin down the exact sources of background noise, and the statistics of the fluctuations are even more difficult to quantify. In SCFM experiments we found that the fluctuations in the RTD were approximately Gaussian [20] in conformance with a theoretical model that was presented in [17]. For the CCFM, an analogous calculation can be carried out, albeit with some careful approximations which can be made, by a consideration of the various time scales inherent in the system. Specifically, we assume that the individual points in the scatter

plot (8) (corresponding to the averaging of several RTDs in an observation window) can be modeled as the response to an external dc magnetic flux that is Gaussian distributed but does not change rapidly (specifically, it changes on time scales that are on the order of the observation window, typically 0.1 s); we also assume that no other noise sources are present. In other words, we assume that each of the window-averaged data points in this figure is a random variable that is uncorrelated with its predecessor, and arises from a different realization of the external signal, these realizations being drawn from a Gaussian distribution with mean ε and variance σ^2 . We are, then, led to a derivation of the statistics (in particular, the first two moments) of the residence times in the two stable steady states of each of the ferromagnetic magnetic cores, whence a simple expression for the resolution can be computed, following the definition (8). While the details of the calculation are beyond the scope of this paper it is worth noting that the resulting expression reproduces, qualitatively, several features that are seen in the experiments; most importantly, the resolution is independent of the target signal in the small signal limit, and depends solely on the (deterministic) device parameters (c , λ) as well as the variance σ^2 of the fluctuations. It also displays the N -dependent performance enhancement that can be expected through the AO configuration (6).

4. Discussion and conclusions

We have developed a laboratory version of the CCFM with the AO configuration. This sensor yields dynamic behavior that faithfully follows all the theoretical predictions. The (laboratory) resolution of this sensor is around 200 pT. In principle, the resolution can be improved (i.e. the numerical value decreases) by incorporating a larger number of cores; this is readily apparent when we realize that the denominator of (8) scales, linearly, as N . However, increasing the number of cores comes at the cost of increased engineering complexity, and additional onboard power (for the coupling circuitry). In addition, the effects of increasing N on the magnetic noise floor are still under investigation, although the results shown in figure 7 provide grounds for optimism that increasing N will not degrade the response as long as we operate within well-defined regimes of optimal response (e.g. near the onset of oscillations as suggested in figure 7). Here, however, an important *caveat emptor* must be inserted. When the system is tuned very close to the onset of oscillations, the background noise can have a significant effect, particularly if it is large enough so that its variance approaches the energy barrier height. This is the weak coupling regime wherein the input to each element from the element it is coupled to is deterministic but very small compared to the noise floor. In this regime an experimental time series of the response displays a noise component that decreases as the coupling becomes larger. Accordingly, while the system may exhibit its best (theoretical) response in the low-frequency regime, a practical system may need to be operated somewhat farther away from the critical point; this option is not available in the SCFM where a large noise floor is, usually, offset by increasing the bias signal amplitude at the cost of a larger onboard power

requirement. Clearly, this makes the case for using every available means to *a priori* lower the system noise floor.

The CCFM draws greater power than its SCFM counterpart. This is, largely, due to the coupling circuitry; in fact N cores must be driven instead of one (in the SCFM). However this is balanced by significantly enhanced performance, quantified by the resolution as well as the experimentally observed lower (compared to the SCFM) noise-floor. Future plans call for the realization of these circuits in low power CMOS which should lead to a reduction in the power budget. In both sensors (CCFM and SCFM), following the nulling procedure, the sensor detects very small static magnetic fields (which can be far below the terrestrial magnetic field) in motion. The observation/measurement time is 0.1 s for both sensors, and it is not necessary to carry out the nulling procedure prior to every observation.

We also point out that, in recent laboratory realizations of the CCFM, parameter mismatch issues have been reduced to a minimum. The cores are near-identical (cut from the same sample of single-domain magnetic wire), and the coupling circuitry can also be set up so that the coupling coefficients λ are almost the same throughout the arrangement. Hence, while there are likely to be lingering mismatches in parameter values, they can be substantially minimized; a recent article [30] addresses, quantitatively, the effects of parameter mismatch specifically variations in the nonlinearity parameter c . Of greater concern are the sources of noise arising from the readout electronics, the magnetic noise in the cores themselves, and fluctuations that are superimposed on the target signal. Magnetic noise in the cores is overcome by very careful fabrication and machining of the single-domain wire that constitutes each core, while the other sources of fluctuations can be modeled using a ‘coarse-grained’ approach (in this case, assuming that they occur on the time scale of the observation time). We also point to our earlier work [23, 28] in which we described the effects of the fluctuations without the above time-scale restriction, and also described some rich noise-mediated spatio-temporal behavior in large coupled rings. This leaves us with another potential source of noise that can easily arise in practice, namely temperature fluctuations that affect the nonlinearity parameter c , particularly when the same device is operated in greatly different environments. The parameter c is proportional to the ratio T_c/T , T_c being the Curie temperature. Temperature fluctuations will, therefore, introduce complicated state-dependent noise terms in the coupled dynamics. In turn, the parameters λ_c as well as the positions of the fixed points of the core potential functions (for zero coupling) will also fluctuate. A systematic treatment of the effects of these fluctuations is beyond the scope of this paper.

It should be clear that our coupling scheme is quite readily applicable to a vast array of dynamical systems which follow the basic ‘particle-in-potential’ paradigm with U being any bi- or multi-stable potential and x the appropriate state variable. The ability to control the oscillation frequency (the laboratory realization of the CCFM can be made to oscillate at frequencies ranging from a few Hz to several kHz, for example) dramatically broadens the range of applications that can benefit

from this scheme. We note, also, that the response of the CCFM to time-sinusoidal magnetic fields has been described (and quantified in the laboratory) [29]. Hence, although we have focused on the case of a dc target signal in this review, we emphasize that there is a richness of nonlinear dynamic behavior that can be exploited in the detection of time-periodic magnetic fields, using the CCFM.

Acknowledgments

We gratefully acknowledge support from the US Office of Naval Research, Code 30.

References

- [1] See e.g. Geyger W 1964 *Nonlinear Magnetic Control Devices* (New York: McGraw-Hill)
- [2] Ripka P 1992 *Sensors Actuators A* **33** 129
- [3] Bornhofft W and Trenkler G 1989 *Sensors, A Comprehensive Survey vol 5* ed W Gopel, J Hesse and J Zemel (New York: VCH)
- [4] Primdahl F 1970 The fluxgate mechanism, part I: the gating curves of parallel and orthogonal fluxgates *IEEE Trans. Magn.* **6** 376
- [5] Ripka P 2001 *Magnetic Sensors and Magnetometers* (Boston, MA: Artech House)
- [6] See e.g. Barone A and Paterno G 1982 *Physics and Applications of the Josephson Effect* (New York: Wiley)
- [7] Clarke J 1993 *SQUIDS: theory and practice The New Superconducting Electronics* ed H Weinstock and R Ralston (Dordrecht: Kluwer)
- [8] See e.g. Bungen I and Prohescu M 1984 *Physics of Solid Dielectrics* (New York: Elsevier)
- [9] Damjanovic D, Muralt P and Setter N 2001 Ferroelectric sensors *IEEE Sensors* **1** 191
- [10] See e.g., Fraden J 1997 *Handbook of Modern Sensors* (New York: AIP Press) and references therein
- [11] Bornhofft W and Trenkler G 1992 *Sensors, A Comprehensive Survey* vols 1, 2 ed W Gopel, J Hesse and J Zemel (New York: VCH)
- [12] Kaluza F, Gruger A and Gruger H 2003 New and future applications of fluxgate sensors *Sensors Actuators A* **106** 48
- [13] Tipek A, Ripka P, O'Donnell T and Kubik J 2004 PCB technology used in fluxgate sensor construction *Sensors Actuators A* **115** 286
- [14] Dezuari O, Belloy E, Gilbert S E and Gijs M A M 2000 Printed circuit board integrated fluxgate sensor *Sensors Actuators A* **81** 200
- [15] Kejik P, Chiesi L, Janossy B and Popovic R S 2000 A new compact 2D planar fluxgate sensor with amorphous metal core *Sensors Actuators A* **81** 180
- [16] Chiesi L, Kejik P, Janossy B and Popovic R S 2000 CMOS planar 2D micro-fluxgate sensor *Sensors Actuators A* **82** 174
- [17] Gottfried R, Budde W and Ulbricht S 1995 *Proc. Transducers'95 Eurosensors*
- [18] Koch R, Deak J and Grinstein G 1999 Fundamental limits to magnetic-filed sensitivity of fluxgate magnetic field sensors *Appl. Phys. Lett.* **75** 3862
- [19] Gordon D and Brown R 1972 *IEEE Trans. Magn.* **8** 76
- [20] Russell C, Elphic R and Slavin J 1979 *Science* **203** 745
- [21] Lenz J 1990 *IEEE Proc.* **78** 973
- [22] Snare R and Means J 1997 *IEEE Trans. Magn.* **13** 1107
- [23] See e.g. Koch C 1999 *Biophysics of Computation* (New York: Oxford University Press)
- [24] Bulsara A, Seberino C, Gammaitoni L, Karlsson M, Lundqvist B and Robinson J W C 2003 Signal detection via residence times asymmetry in noisy bistable devices *Phys. Rev. E* **67** 016120
- [25] Striker S and Wulkan A 1961 A pulse position type magnetometer *Trans. IEE* **80** 253-8
- [26] Ando B, Baglio S, Bulsara A and Sacco V 2005 RTD based fluxgate magnetometers *IEEE Sensors* **5** 895
- [27] Ando B, Baglio S, Bulsara A and Sacco V 2005 Theoretical and experimental investigations on residence times difference fluxgate magnetometers *Measurement* **38** 89
- [28] Ando B, Baglio S, Bulsara A and Sacco V 2005 Effects of driving mode and optimal material selection on a residence times difference-based fluxgate magnetometer *IEEE Trans. Instrum. Meas.* **54** 1366
- [29] In V, Bulsara A, Palacios A, Longhini P, Kho A and Neff J 2003 *Phys. Rev. E* **68** 045102
- [30] Bulsara A, In V, Kho A, Longhini P, Palacios A, Rappel W-J, Acebron J, Baglio S and Ando B 2004 Emergent oscillations in unidirectionally coupled overdamped bistable systems *Phys. Rev. E* **70** 036103
- [31] Lindner J and Bulsara A 2006 One-way coupling enables noise-mediated spatiotemporal patterns in media of otherwise quiescent multistable elements *Phys. Rev. E* **74** 020105
- [32] Palacios A, Aven J, In V, Longhini P, Kho A, Neff J and Bulsara A 2007 Coupled core fluxgate magnetometer: novel configuration scheme and the effects of a noise-contaminated external signal *Phys. Lett. A* **367** 25
- [33] Chiriac H, Yamasaki J, Ovari T A and Takajo M 1999 Magnetic domain structure in amorphous glass-covered wires with positive magnetostriction *IEEE Trans. Magn.* **3** 3901
- [34] Ando B, Baglio S, Sacco V, Bulsara A and In V 2008 PCB fluxgate magnetometers with a residence times readout strategy: the effects of noise *IEEE. Trans. Instrum. Meas.* **57** 19
- [35] Koch R and Rozen J 2001 Low noise fluxgate magnetometers using ring and rod core geometries *Appl. Phys. Lett.* **78** 1897
- [36] Bulsara A, Lindner J, In V, Kho A, Baglio S, Sacco V, Ando B, Longhini P, Palacios A and Rappel W-J 2006 Coupling-induced cooperative behavior in dynamic ferromagnetic cores in the presence of a noise floor *Phys. Lett. A* **353** 4
- [37] In V, Bulsara A, Palacios A, Longhini P and Kho A 2005 Complex dynamics in unidirectionally coupled overdamped bistable systems subject to a time-periodic external signal *Phys. Rev. E* **72** 045104
- [38] In V, Palacios A, Hernandez M, Longhini P, Kho A and Bulsara A 2008 Coupling-induced oscillations in nonhomogeneous, overdamped, bistable systems *Phys. Lett. A* **372** 4381-7